Fast ion transport in the quasi-single helical reversed-field pinch

Cite as: Phys. Plasmas **26**, 022502 (2019); https://doi.org/10.1063/1.5084059
Submitted: 03 December 2018 . Accepted: 10 January 2019 . Published Online: 04 February 2019

P. J. Bonofiglo, J. K. Anderson, M. Gobbin, D. A. Spong, J. Boguski, E. Parke, J. Kim, and J. Egedal

Physics of Plasmas ARTICLE scitation.org/journal/php

Fast ion transport in the quasi-single helical reversed-field pinch

Cite as: Phys. Plasmas **26**, 022502 (2019); doi: 10.1063/1.5084059
Submitted: 3 December 2018 · Accepted: 10 January 2019 ·
Published Online: 4 February 2019

P. J. Bonofiglo,[1,a),b)] J. K. Anderson,[1] M. Gobbin,[2] D. A. Spong,[3] J. Boguski,[1] E. Parke,[4] J. Kim,[1] and J. Egedal[1]

AFFILIATIONS

[1]University of Wisconsin-Madison, Madison, Wisconsin 53706, USA
[2]Consorzio RFX, Associazione Euratom-ENEA sulla Fusione, Padova 35127, Italy
[3]Oak Ridge National Laboratory, Oak Ridge, Tennessee 37831, USA
[4]TAE Technologies Inc., Foothill Ranch, California 92610, USA

Note: This paper is part of the Special Collection: Papers from the 60th Annual Meeting of the APS Division of Plasma Physics.
Note: Paper YI2 4, Bull. Am. Phys. Soc. **63** (2018).
[a)]Invited speaker.
[b)]**Electronic mail:** bonofiglo@wisc.edu

ABSTRACT

The reversed-field pinch (RFP) can spontaneously transition from an axisymmetric magnetic topology to a 3D-helical geometry. Investigations on fast ion transport associated with energetic particle driven Alfvén instabilities, tearing mode induced stochasticity, and neoclassical effects have been performed on the Madison Symmetric Torus. STELLGAP produced shear-Alfvén continua seeded with V3FIT 3D-equilibrium reconstructions describe the response of Alfvénic bursting activity as a direct consequence of the equilibrium change on the fast ion resonance. Far infrared interferometry resolved electron density perturbations associated with the bursts provide a spatial measurement of the mode structure and support the reconstructions. The bursts produce no global resonant fast ion transport; however, their disappearance at a high core-resonant amplitude implies other transport mechanisms at play. Neutral particle analysis and neutron signals suggest fast ion losses at sufficient core tearing mode strength, supporting the lack of Alfvénic activity. The guiding-center code ORBIT corroborates rapid fast ion loss times in the helical state largely as a consequence of remnant tearing modes. Additionally, ORBIT simulations demonstrate little neoclassical enhancement of particle transport. While superbanana orbits may exist, the growth in the core-resonant fast ion island and the associated secondary mode overlap govern the largest transport process, leading to robust fast ion losses in the 3D-RFP.

I. INTRODUCTION

Empirically, at adequately high Lundquist number, $S = \frac{Lv_A}{\eta} \sim \frac{I_p T_e^{3/2}}{\sqrt{n_e}} \sim 10^6$, the reversed-field pinch transitions from a 2D-axisymmetric equilibrium to a 3D-helical equilibrium known as quasi-single helicity (QSH). A helical axis forms when the innermost resonant tearing mode grows and envelops the magnetic axis, while the secondary modes maintain, or decrease, their amplitudes. Typically, a broad spectrum of $m = 1$ poloidal tearing modes govern reversed-field pinch (RFP) plasmas as a direct consequence of the RFP's relatively low safety factor ($q < 1$). Therefore, the standard RFP may be denoted as a multiple helicity (MH) state. In the Madison Symmetric Torus (MST), plasmas transition to the QSH state in non-reversed discharges [$q(a) = 0$] at a modest I_p (>350 kA) and low density ($\bar{n}_e < 0.5 \times 10^{13}$ cm^{-3}) with $m = 1$, $n = 5$ as the dominant perturbation. Thus, a 5-fold toroidal periodicity defines the helical equilibrium. The spectral index, $N_s = [\sum_n (\frac{\tilde{b}_n^2}{\sum_n \tilde{b}_n^2})^2]^{-1}$, provides a useful parameter to help identify this state, where $\tilde{b}_n$ denotes the tearing mode amplitudes and $N_s \lesssim 1.2$ represents the QSH state. Depending on the plasma conditions, QSH plasmas in MST saturate at $\frac{\tilde{b}_5}{|B|} \sim 5\%$–$8\%$ with the secondary tearing mode amplitudes in total around 0.5%–2%.

Prior research has shown that thermal particles experience enhanced confinement in the helical RFP.[1–4] This presents a possible avenue for a new magnetic confinement fusion scheme.[5]

Little attention has been placed on the fast particle content, however, equally critical for fusion. Therefore, the behavior of fast ions in the QSH state poses a critical question for the helical RFP's fusion relevance and mandates a comprehensive experimental and computational investigation.

The neutral beam injector (NBI) on MST is oriented tangentially, producing core-localized, high-pitch, 25 keV hydrogen or deuterium ions for analysis. The NBI deposited fast ions in MST mimic alpha particles in a burning reactor and act as a testbed for energetic particle physics in the 3D-RFP.[6] In comparison to alpha particles in a RFP-like reactor, MST's NBI born ions possess a similar gyroradius relative to the device size ($\rho_{fi}/a \sim 0.1$), superthermal speed ($v_{fi}/v_{th} \sim 13$), and superalfvénic speed ($v_{fi}/v_A > 1$) but form a localized pitch-angle distribution due to the injection geometry in comparison to alpha particles' isotropic distribution.[7] The MST device ($R_0 = 1.5$ m and $a = 0.5$ m) produces deuterium RFP plasmas with total current $I_p = 200$–600 kA, central field strength $|B| = 0.2 - 0.5$ T, and confined electron temperature $T_e(0) = 200 - 2000$ eV.

In the axisymmetric RFP, fast ions are well confined due to substantial in-surface guiding-center drifts that allow the particle to ignore tearing mode induced magnetic stochasticity.[8] The fast ions obtain classical confinement with weak slowing collisions on the electrons. Neoclassical effects, such as banana orbits, are non-existent in the standard RFP in part due to that the RFP's relatively weak magnetic field results in a fast ion Larmor radius larger than the banana width ($r_L \sim \Delta_b$).

Conversely, when considering contours of mod B, the helical RFP bears similarities to both unoptimized stellarators and tokamak field ripples which are prone to neoclassical effects.[9–13] One may therefore expect that the RFP's helical perturbation will result in similarly strong fast ion transport. The break in ϕ-symmetry leads to the non-conservation of the toroidal canonical angular momentum given by

$$p_\phi = mRV_\phi + e\psi_p, \tag{1}$$

where ψ_p represents the poloidal flux and V_ϕ the toroidal velocity. In tokamaks and stellarators, the loss of toroidal symmetry allows secondary particle trapping, where superbanana orbits may undergo strong radial drifts and drive rapid particle losses.[14,15] Research on thermal particles in the RFP's helical ripple failed to observe unoptimized stellarator-like losses.[16] The superbanana regime only became significant at experimentally unobtainable perturbation levels. Thus, at the first glance, the investigation of fast ions in the QSH state necessitates the examination of any neoclassical transport effects. As will be discussed, the transport associated with Alfvénic activity and tearing modes also warrants exploration, with the latter mechanism proving central to fast ion losses.

This work provides an analysis of fast ion transport in the helical RFP device. Our experimental measurements, corroborated by numerical simulations, demonstrate that fast ions undergo drastic losses in the transition to the 3D-equilibrium. Our results suggest that the role of secondary tearing modes supersedes that of neoclassical effects, while resonant mode transport is absent.[17] Although the toroidal symmetry breaking of the dominant $n = 5$ helical perturbation resembles that of an unoptimized stellarator, fast ions largely lack the superbanana regime of the neoclassical transport theory due to the RFP guiding-center drifts. This paper aims to explain the dominant fast ion transport mechanisms so as to better understand and mitigate the observed losses.

II. ALFVÉN MODE INDUCED TRANSPORT

MST's NBI produces enough fast ion pressure to excite Alfvén instabilities.[18] These instabilities occur at a resonance with the shear-Alfvén continuum, $\omega = k_\parallel v_A$, with the drive supplied from the energetic particle population.[19] In the standard RFP, these instabilities typically present themselves in a periodic bursting nature at a constant frequency. With the transition to the 3D-equilibrium marked by the growth in the dominant $n = 5$ tearing mode amplitude, however, the energetic particle driven bursts on the associated $n = 5$ branch of the Alfvén continuum rise in frequency. An example spectrogram of the observed Alfvénic activity coupled with tearing mode amplitudes is shown in Figs. 1(a) and 1(b) with the $n = 5$ mode velocity in part (c). A strong relationship between burst frequency and normalized core-tearing mode amplitude is presented in part (d) for a given beam species. Figure 1 presents some interesting observations: the well-established connection between burst frequency and core-resonant amplitude, the appearance of two frequency branches for deuterium fueled NBI, and the cessation of bursts at a correspondingly high amplitude.

An 11-chord Far infrared (FIR) interferometry system on MST provides spatial measurements of the Alfvén instabilities through correlations between electron density perturbations associated with the wave induced magnetic fluctuations.[21,22] The spectral coherence between the density and magnetic fluctuations is given by

$$\gamma = \sqrt{\frac{|\langle \mathcal{F}_{\tilde{b}} \mathcal{F}_{\tilde{n}} \rangle|^2}{\langle |\mathcal{F}_{\tilde{b}}|^2 \rangle \langle |\mathcal{F}_{\tilde{n}}|^2 \rangle}}, \tag{2}$$

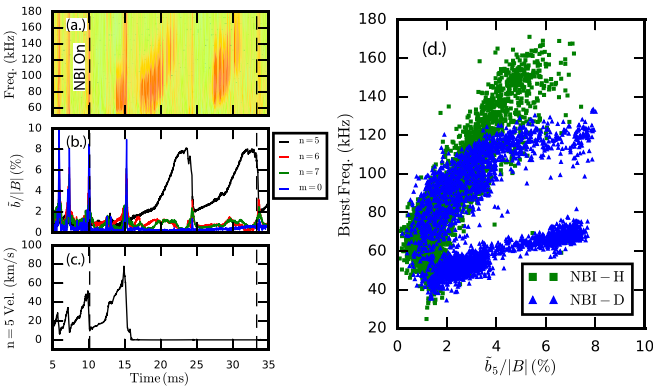

FIG. 1. (a.) Spectrogram produced from edge magnetic coils showing the $m = 1$, $n = 5$ bursting activity where the dashed vertical lines mark the NBI turn on and off (b.) Dominant ($m = 1$, $n = 5$) and secondary ($m = 1$, $n = 6$–7 and $m = 0$, $n = 4$) tearing mode amplitudes (c) $n = 5$ phase velocity (d) Relationship between normalized core-tearing mode amplitude and burst frequency for hydrogen and deuterium fueled NBI. [Associate Dataset available at https://doi.org/10.5281/zenodo.2547914] (Ref. 20).

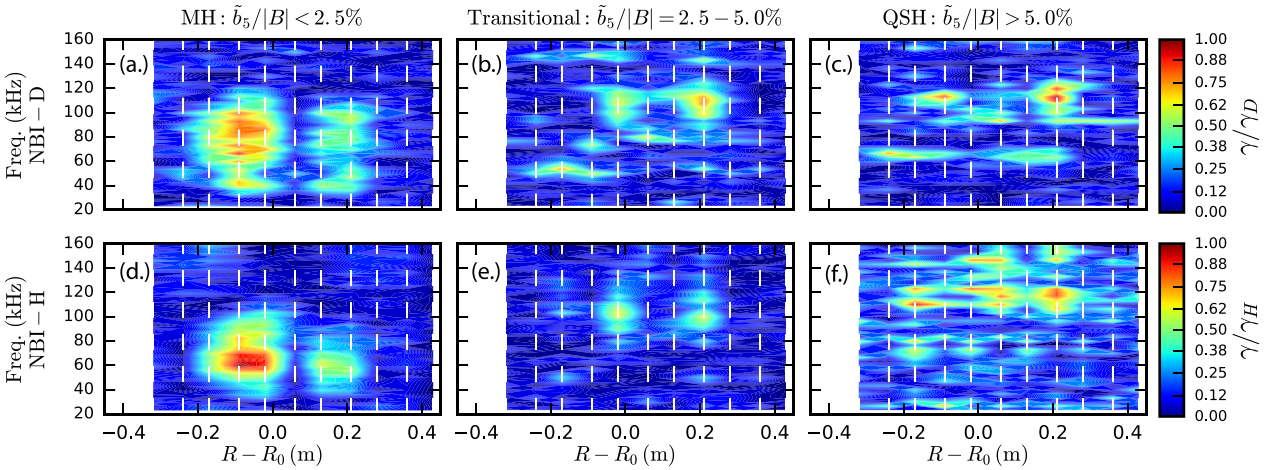

FIG. 2. The spectral coherence between electron density perturbations and magnetic fluctuations from deuterium driven Alfvén instabilities (a)–(c) and hydrogen driven (d)–(f). The coherences are normalized relative to their maxima of $\gamma_D = 0.25$ and $\gamma_H = 0.32$. Looking from left to right, the associated bursts are ensembled according to the normalized core-resonant amplitudes of: <2.5%, 2.5%–5%, and >5%, respectively. The dashed-vertical lines represent the FIR chords. [Associate Dataset available at: https://doi.org/10.5281/zenodo.2547914] (Ref. 20).

where $\mathcal{F}$ represents the associated Fourier transform and $\langle\ \rangle$ denotes an ensemble average over the Alfvénic bursts. Figure 2 presents the spectral coherence for hydrogen and deuterium injected fast ions in three topologies: the MH state, a transitional state, and the QSH state. Again, the observed rise in burst frequency clearly presents itself, and the deuterium driven bursts display distinct structures for the observed low and high frequency branches. Additionally, the coherence structures undergo an outward, radial shift indicative of a strong fast ion population in the newly forming helical axis.

The shear-Alfvén continuum was calculated with the STELLGAP code across a variety of helical perturbation strengths utilizing three dimensional equilibria created with the V3FIT reconstruction code.[23–25] Figure 3 displays the resultant q-profiles and $n = 5$ Alfvén continua. As the topology transitions from the MH to QSH regime, the q-profile becomes non-monotonic and shrinks. The Alfvén continuum responds with a branch that forms a local minimum that rises with the corresponding change in q. Mapping the FIR measurements onto the STELLGAP continua, the Alfvénic modes first occur near the core then shift to around 0.2 in units of normalized poloidal flux. The evolving 3D-equilibrium alters the Alfvén continuum in such a manner so as to preserve the energetic particle distribution near the core. With the NBI deposition being the strongest in the core, the fast ion spatial gradient and resonance allow the bursts to up-shift in frequency and maintain a region for instability growth throughout the topological evolution.

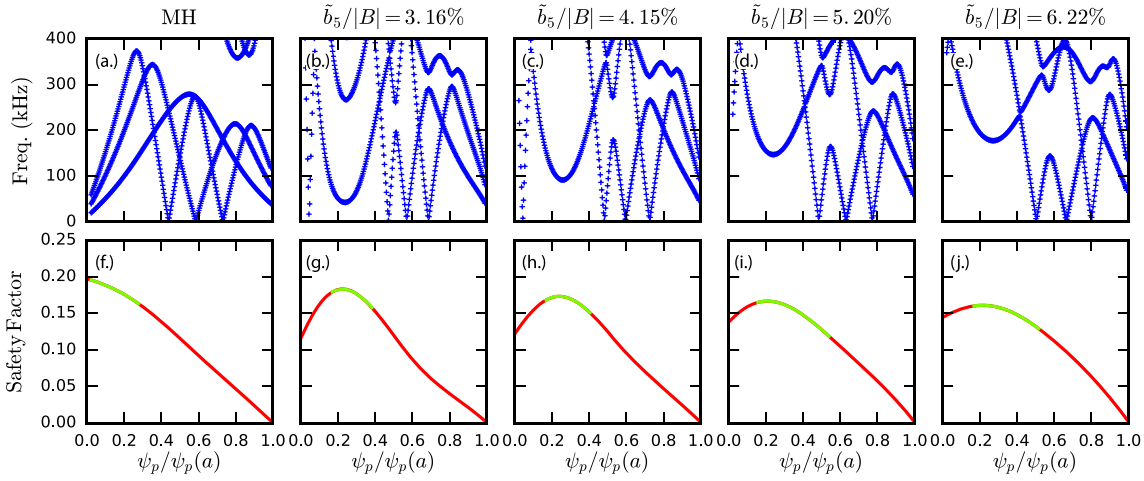

FIG. 3. (a)–(e) Shear-Alfvén continua produced from the code STELLGAP and their associated q-profiles (f)–(j) from V3FIT reconstructions. Looking from left to right, the normalized core-resonant strengths are: 1.7%, 3.2%, 4.2%, 5.2%, and 6.2%, respectively. (a) and (f) Denote a standard MH RFP while all others represent varying strengths of QSH. The regions highlighted in green identify the mapped NBI deposition and measured FIR resonance locations. [Associate Dataset available at: https://doi.org/10.5281/zenodo.2547914] (Ref. 20).

The minima in the Alfvén continua strongly suggest the possibility of discrete gap modes such as GAEs, RSAEs, or even low frequency BAEs.[19] With reference to the observed branches in Fig. 1(d), the continua minima establish regions of near zero continuum damping $\left(\frac{d\omega}{dr} \sim 0\right)$. Alfvén modes may then present themselves at varying frequencies so long as the fast ion resonance is satisfied. For fixed beam energy, the higher velocity hydrogen ions are theorized to resonate less efficiently with the low frequency modes compared to the slower deuterium ions.

With regard to fast ion transport, although the bursts result in a localized re-distribution of the fast ions, they have little observed effect on the global particle content. Neutron flux measurement ensembles confirm this and show no marked difference in the presence of energetic particle instabilities. Figure 4 shows that the bursting modes themselves do not cause a significant change in the global neutron flux at less than the 1% level. The redistribution of the fast ions associated with the bursting events is localized to the core, conserving the overall volume integration of the particle content.[26] Indeed, the bursting nature of the destabilized modes follows predator-prey relaxation oscillations characteristic of localized fast ion transport.[22] The absence of bursts at a high core-resonant mode amplitude shown in Fig. 1(a) suggests a lack of drive from the fast ion distribution, hinting at fast ion losses. The neutron flux ensembles, however, demonstrate that the bursting AEs produce negligible losses. These results hold true regardless of the strength of the helical perturbation as well. Thus, even though one may infer information about the evolving helical equilibrium from the response of the energetic particle driven Alfvén modes, the modes themselves result in no substantial particle transport.

III. TEARING MODE INDUCED TRANSPORT

The response of the fast ion content throughout the transitioning equilibrium was monitored with neutron flux measurements produced from DD-fusion events. The neutron signals support the notion of fast ion losses in the QSH state as mentioned in Sec. II. Figure 5(a) displays the normalized rate of change of the global neutron flux as a function of the tearing mode amplitudes. One finds that the fast ion driven neutron flux decreases with the large core-resonant mode and weak secondary mode amplitudes. Interestingly, the neutron flux experiences a more rapid decrease in the presence of secondary tearing modes in the QSH regime compared to the MH, depicted in Fig. 5(b). This suggests that the remnant tearing modes might play a more important role in the helical RFP than the standard RFP.

Similarly, neutral particle analysis measurements resulting from fast ion charge-exchange losses decrease during the helical state.[6] Both tangential and radial lines of the site show distinct decreases with the growth in the $n=5$ core-resonant mode amplitude. The neutral particle analyzer signal is a line-averaged measurement highly sensitive to particle pitch and neutral density. This makes for a difficult interpretation of the signal in the helical RFP. In comparison to the neutron signals, no strong dependence on secondary tearing modes has been observed. It is worth mentioning that as the $n=5$ mode amplitude grows, eddy-currents in the MST's conducting shell provide a torque which slow and lock the plasma to the wall at a fixed phase.[27] Externally applied resonant magnetic perturbations (RMPs) aid in locking and allow for experimental phase control of the helical core for preferential diagnostic viewing.[28] Of note, no fast ion measurements were found to have any associated phase dependence. This is likely a result of the injection geometry of MST's NBI depositing fast ions across a full helical period, averaging over any phase dependence.

The direct measurement of the global fast ion confinement time, τ_{fi}, was obtained on MST with the beam-blip technique via the associated neutron flux decay.[29] The confinement time measurements confirm fast ion loss during the transition to QSH and reveal the importance of the secondary tearing modes. The results are plotted as a function of normalized core-resonant amplitude in Fig. 6(a). Fast ion loss times found from the Hamiltonian guiding-center particle tracking code ORBIT in

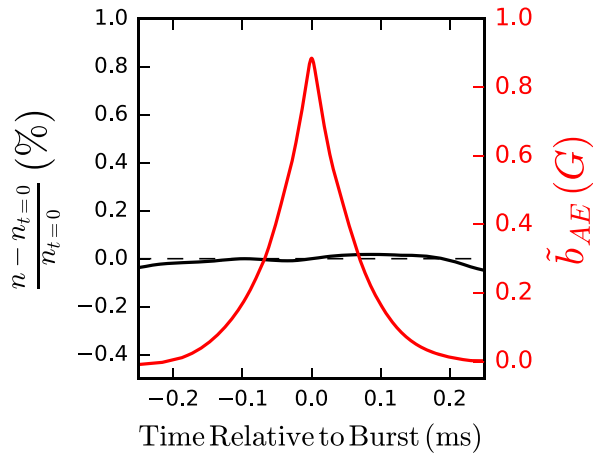

FIG. 4. Normalized change in global neutron flux (black) and AE burst amplitude (red) with respect to bursting time for ensembled, deuterium driven AE bursts. [Associate Dataset available at: https://doi.org/10.5281/zenodo.2547914] (Ref. 20).

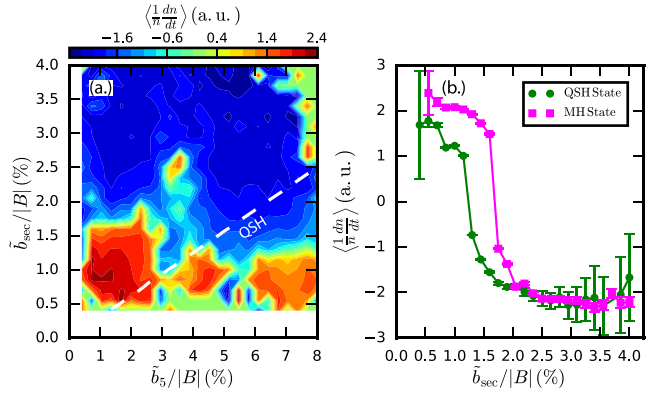

FIG. 5. (a.) Ensemble average of the normalized rate of change of the global neutron flux with the dashed area representing the QSH regime of $N_s < 1.2$. (b.) Line cuts of the ensembled neutron flux rate as a function of the normalized secondary tearing mode amplitude for the QSH ($\tilde{b}/|B| = 6.7\%$) and MH ($\tilde{b}/|B| = 1.7\%$) states. [Associate Dataset available at: https://doi.org/10.5281/zenodo.2547914] (Ref. 20).

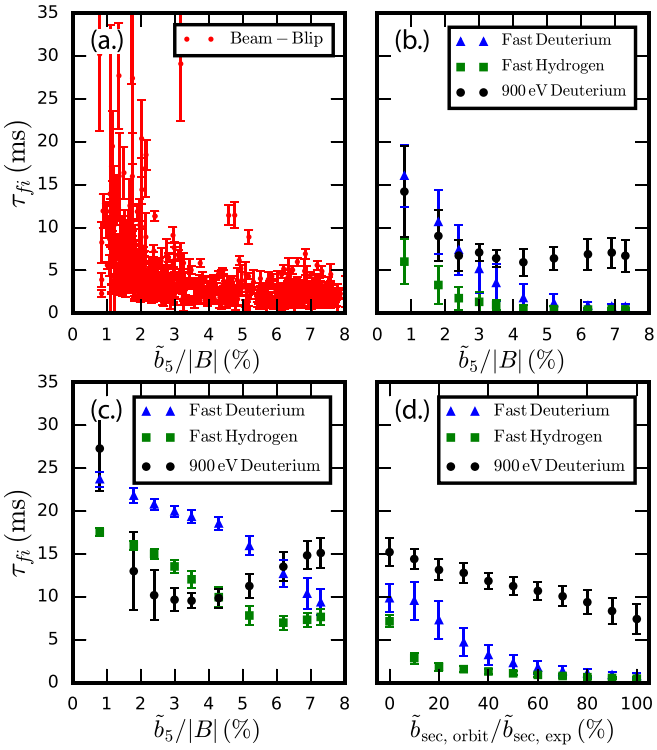

FIG. 6. (a) Experimental τ_{fi} measured via the beam-blip technique on MST (b) Simulated τ_{fi} from ORBIT with $m=1$, $n=5$–16 and $m=0$, $n=1$–4 modes active (c) Simulated τ_{fi} from ORBIT simulations in a SHAx state with only the $m=1$, $n=5$ mode active (d) Simulated τ_{fi} as a function of scaled secondary mode amplitudes from ORBIT simulations with $\tilde{b}_5/|B| \approx 7\%$. [Associate Dataset available at: https://doi.org/10.5281/zenodo.2547914] (Ref. 20).

a variety of simulated settings are also plotted in parts (b)–(d).[30] Figure 6(b) shows the simulated fast ion loss times throughout the transition to a QSH state in settings that come as close as possible to mimicking experiment. The simulated results match those measured and follow the same marked decrease with the transition from the standard RFP to the 3D-RFP. Figure 6(c) removes all modes with the exception of the $m=1$, $n=5$ mode, producing an ideal, single-helical axis (SHAx) topology at a high core-resonant mode amplitude. Compared to the QSH state, the simulated SHAx case results in drastic improvement of the fast ion confinement. Therefore, fast ion confinement and transport in the 3D-RFP strongly depends on the role of the secondary modes. Part (d) of Fig. 6 presents τ_{fi} as a function of the scaled secondary mode amplitudes at a fixed normalized core-resonant amplitude of 7%. This represents the transition from an ideal SHAx state to QSH and serves to quantify the degree at which the secondary modes take over. At the slightest presence of secondary modes (~30% of their experimental values), we find a rapid convergence to severe QSH-like losses.

The fast ions still observe some degree of de-coupling from the standard RFP's magnetic stochasticity. Figure 7 presents toroidally projected Poincaré plots for 25 keV deuterium ions at varying levels of the helical perturbation. Part (a) represents a typical MH state with strong fast ion confinement. The well-defined fast ion phase-space structures near the core demonstrate reduced fast ion transport despite the presence of large magnetic stochasticity. With the growth in the $n=5$ tearing mode, however, the $n=5$ fast ion island grows, as shown in parts (b) and (c). At a large core-resonant amplitude, the fast ion phase-space structures near the core, representing the particle conservation, erode and, ultimately, disappear. The growth in the $n=5$ tearing mode results in a slight reduction in fast ion confinement as particles are more easily transported outward by the larger island width. In the QSH state, secondary modes greatly enhance the transport due to their additional, significant overlap, resulting in considerable losses. Naturally, this appears to be a form of Rechester-Rosenbluth like transport where the magnetic chaos has propagated to fast ion phase-space.[31] Further transport studies are ongoing to identify the characteristic $D \sim \tilde{b}^2$ scaling.

IV. NEOCLASSICAL TRANSPORT

The hypothesis that the helical RFP possesses similar neoclassical transport to that of an unoptimized stellarator proved to be incorrect. Helically trapped superbanana orbits may occur in the QSH state, but little radial transport occurs due to the RFP's well-natured guiding center drifts.[8] While the perturbation levels reach a maximum of approximately 7%–8%, the equilibrium field still dominates the particle drifts. In that regard, the

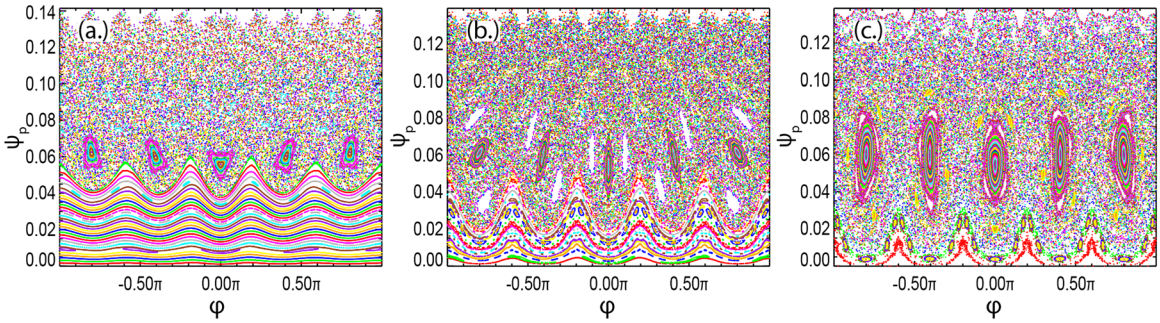

FIG. 7. Fast ion Poincaré phase-space plots produced with ORBIT for 25 keV deuterium ions at normalized core tearing mode amplitudes of (a) 0.8% (b) 4.3% (c) 7.5%. Parts (a)–(c), respectively represent MH, transitional, and QSH states. [Associate Dataset available at: https://doi.org/10.5281/zenodo.2547914] (Ref. 20).

grad-B drift is the strongest in the RFP and is normal to the flux surfaces everywhere, meaning that any helically trapped particle will not undergo outward drifts. ORBIT was used to further probe for any trace of neoclassical transport effects on the fast ion population.

Volume averaged diffusion coefficients found analogous to those of Gobbin *et al.* lacked the $1/\nu$ dependence created from superbanana orbits.[11,16] Figure 8 shows ORBIT calculated diffusivity in a SHAx state. The computed diffusivity depicted in Fig. 8 monotonically increases with collisionality, eventually reaching the classical limit, $D_{cl} = \rho^2\nu$, where ρ is the Larmor radius. While the presence of the large $m = 1, n = 5$ mode allows for helical trapping of fast ions and the existence of superbanana orbits, their effect appears to be lacking. While performing these ORBIT runs with added secondary modes in a QSH state, the fast ion injection surface became stochastic and greatly complicates the diffusion calculation. Work is ongoing to remedy this problem, but this further illustrates the impact of the secondary tearing modes on fast ion phase-space.

Figure 9(a) pictures the magnetic contours in a QSH topology. The overplotted white lines demarcate a field line trace. The breaking of the toroidal symmetry clearly presents itself in the bands of high-low field strength. The contours qualitatively resemble that of an unoptimized stellarator.[32] Part (b) of Fig. 9 plots the normalized magnetic field strength for the above plotted field line for a number of toroidal transits. Toroidal magnetic wells exist that allow for low-pitch fast ions to become helically trapped and result in superbanana orbits.[33] As mentioned previously, however, the RFP's guiding-center drifts are along flux surfaces, resulting in $\langle \vec{v}_d \cdot \vec{\nabla}\psi \rangle \sim 0$ and little radial transport.[11,34] Thus, one may argue that the helical RFP acts more akin to an omnigenous stellarator in which collisionless trapped trajectories are confined.[31,34–37]

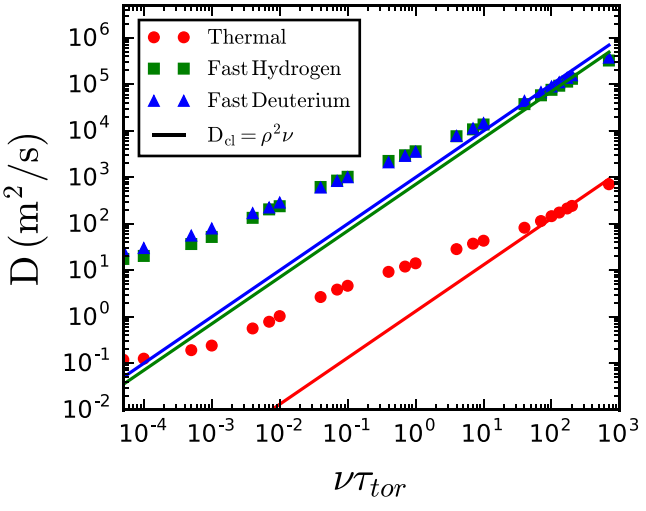

FIG. 8. ORBIT calculated diffusivity as a function of collisionality, ν, normalized to toroidal transit time, τ_{tor}, for fast deuterium and hydrogen ions and thermal deuterons in a SHAx-like topology consisting of only the $m = 1$ and $n = 5$ modes at $\tilde{b}_5/|B| = 7.3\%$. [Associate Dataset available at: https://doi.org/10.5281/zenodo.2547914] (Ref. 20).

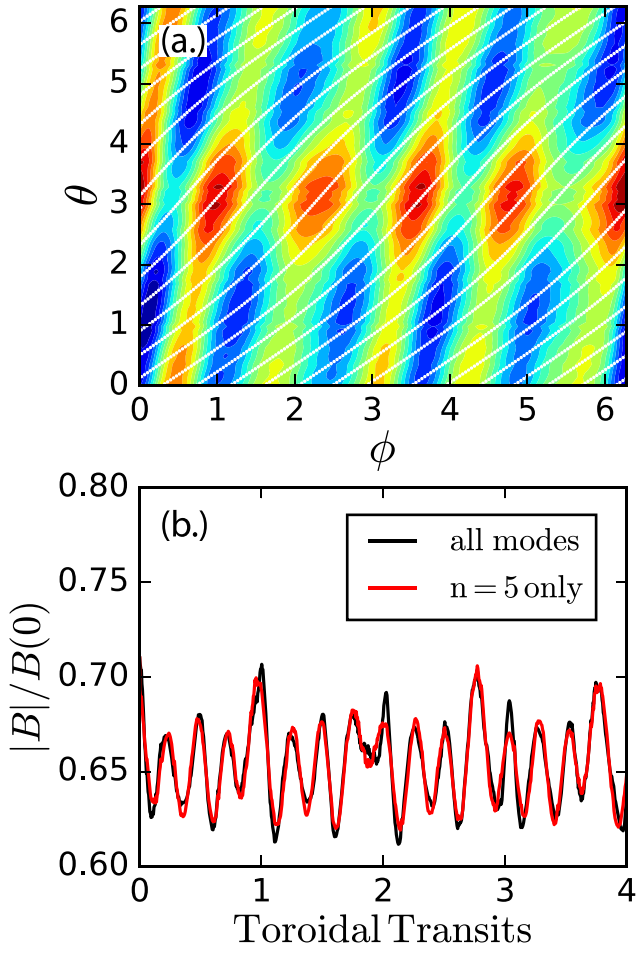

FIG. 9. (a) Contour plot of the magnetic field amplitude in a QSH topology with $\tilde{b}/|B| = 7.0\%$ and all modes present at mid-radius. The white lines denote a field line trace. (b) Magnitude of the magnetic field normalized to the field on axis for the above field line trace in the presence of all tearing modes and only the $m = 1$, $n = 5$ mode. [Associate Dataset available at: https://doi.org/10.5281/zenodo.2547914] (Ref. 20).

The resultant breaking in the toroidal canonical momentum given in Eq. (1) should occur with the presence of superbanana orbits. An ORBIT simulation with 4000 25 keV deuterium test particles was conducted in a QSH topology with collisions turned off. The simulation was performed for two particle groups with different initial conditions. The first group contained particles that replicated MST's NBI deposition and pitch-distribution. The second group was a random Monte-Carlo placement of particles that allowed for the possibility of initial low-pitch fast ions. The toroidal canonical angular momentum was calculated for each particle as a function of time, and the fraction of particles with conserved p_ϕ is shown in Fig. 10 as a function of scaled secondary tearing modes.

While the breaking of p_ϕ occurs weakly for the emergence of the secondary modes, the presence of the lower-pitch fast ions provides the greatest impact on p_ϕ conservation. The low-pitch particles can become trapped in the magnetic wells of

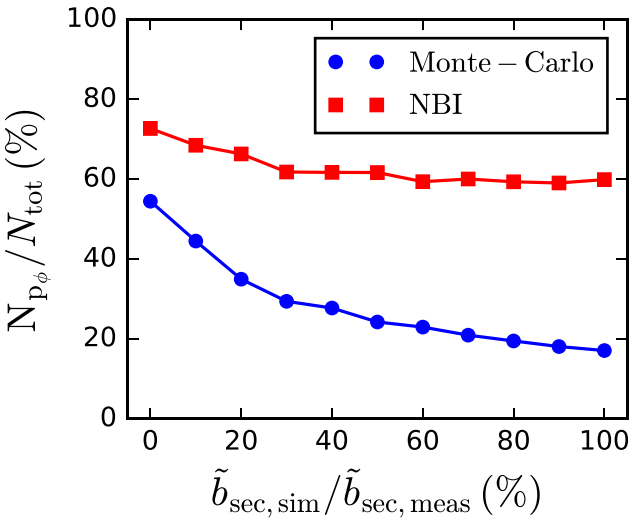

FIG. 10. Fraction of 25 keV deuterium ions with conserved p_ϕ as a function of scaled secondary tearing mode amplitudes as measured in ORBIT simulations. The "NBI" labeled data represents a simulated deposition of particles mimicking that of MST's NBI. The "Monte-Carlo" labeled data represent particles initially seeded within the domain: $\left\{\frac{v_\parallel}{v} \in [0.01, 1.0];\ \frac{\psi_p}{\psi_p(a)} \in [0.1, 1.0];\ \theta \in [0, 2\pi];\ \phi = 0\right\}$. [Associate Dataset available at: https://doi.org/10.5281/zenodo.2547914] (Ref. 20).

Fig. 9(b) and undergo superbanana orbits with non-conserved p_ϕ. Performing a direct orbit trajectory identification on the fast ion guiding-center trajectories discovered the existence of superbanana and banana orbits in the Monte-Carlo initialized particles much more frequently than in the NBI ions, as one expects. While the NBI simulated particles are of a higher-pitch, i.e., co-passing, and experience less neoclassical effects, they are still lost quickly due to the presence of the secondary tearing modes discussed in Sec. III. Thus, the occurrence of helically trapped particles is possible, but, as shown in Fig. 8, they bear no impact on fast ion confinement. The superbanana particles are more likely to be lost through pitch-angle scattering and poloidally drifting out of the magnetic well to co-passing orbits and succumbing to the stochastic fast ion phase-space presented in Fig. 7.[15,34,38]

V. CONCLUSION

In summary, 3D modeling of the helical equilibria and Alfvén continua demonstrate that the frequency shift and radial displacement of energetic particle instabilities are a direct consequence of the evolving equilibrium itself. By mapping FIR coherence measurements onto STELLGAP produced Alfvén continua, energetic particle driven Alfvén instabilities may provide information on the development of the magnetic geometry. The bursting modes have no role in global particle transport, though. Neutron flux and neutral particle analysis measurements support the disappearance of the bursting modes in the QSH state and infer fast ion losses. More so, the neutron signals demonstrate that the fast ions respond more strongly to the secondary tearing modes in the QSH state than the MH state. The beam-blip technique provided direct experimental fast ion loss time measurements and confirms substantial fast ion losses in the 3D-RFP. Corroborating ORBIT simulations illustrate that growth in the dominant $n = 5$ tearing mode coupled with remnant secondary modes are to blame. The helical RFP qualitatively resembles an unoptimized stellarator at first glance, but the well-natured guiding center drifts result in weak neoclassical enhancement to particle transport. In this regard, the QSH state acts as an omnigenous stellarator, where superbanana orbits may be present but have no detrimental effects on confinement.

Overall, while thermal particles experience a reduction in stochasticity and improved confinement, fast ions experience the opposite. Examination into fast ion transport in relation to Alfvén instabilities, tearing mode effects, and neoclassical effects was performed. Remnant tearing mode induced fast ion phase-space stochasticity governs the fast ion confinement more so than trapped particle effects. While this presents an obstacle in the utilization of the QSH regime in a fusion scheme, the secondary mode strengths decrease with Lundquist number scaling, lessening their impact, and may present a consistent scenario for ignition provided the tearing instability falls fast enough with S.[39,40]

ACKNOWLEDGMENTS

This work was supported by the U.S. Department of Energy Office of Science, Office of Fusion Energy Sciences program, under Award No. DE-FC02-05ER54814, and accomplished with the use of the infrastructure of Complex DOL (Budker Institute of Nuclear Physics, Russia).

REFERENCES

[1]I. Predebon, L. Marrelli, R. B. White, and P. Martin, Phys. Rev. Lett. **93**, 0145001 (2004).
[2]R. Lorenzini, D. Terranova, A. Alfier, P. Innocente, E. Martines, R. Pasqualotto, and P. Zanca, Phys. Rev. Lett. **101**, 025005 (2008).
[3]M. Gobbin, D. Bonfiglio, D. F. Escande, A. Fassina, L. Marrelli, A. Alfier, E. Martines, B. Momo, and D. Terranova, Phys. Rev. Lett. **106**, 025001 (2011).
[4]R. Lorenzini, F. Auriemma, A. Fassina, E. Martines, D. Terranova, and F. Sattin, Phys. Rev. Lett. **116**, 185002 (2016).
[5]R. Lorenzini, E. Martines, P. Piovesan, D. Terranova, P. Zanca, M. Zuin, A. Alfier, D. Bonfiglio, F. Bonomo, A. Canton *et al.*, Nat. Phys. **5**, 570 (2009).
[6]J. K. Anderson, W. Capecchi, S. Eilerman, J. J. Koliner, M. D. Nornberg, J. A. Reusch, J. S. Sarff, and L. Lin, Plasma Phys. Controlled Fusion **56**, 094006 (2014).
[7]D. Hill and R. Hazeltine, http://fusion.gat.com/tap/final_report.php/ for "Report of the FESAC Toroidal Alternates Panel," 2008.
[8]G. Fiksel, B. Hudson, D. J. Den Hartog, R. M. Magee, R. O'Connell, S. C. Prager, A. D. Beklemishev, V. I. Davydenko, A. A. Ivanov, and Y. A. Tsidulko, Phys. Rev. Lett. **95**, 125001 (2005).
[9]M. H. Redi, H. E. Mynick, M. Suewattana, R. B. White, and M. C. Zarnstorff, Phys. Plasmas **6**, 3509 (1999).
[10]R. B. White, R. J. Goldston, M. H. Redi, and R. V. Budny, Phys. Plasmas **3**, 3043 (1996).
[11]H. E. Mynick, Phys. Plasmas **13**, 058102 (2006).
[12]D. A. Spong, Phys. Plasmas **22**, 055602 (2015).
[13]P. N. Yushmanov, J. R. Cary, and S. G. Shasharina, Nucl. Fusion **33**, 1293 (1993).
[14]D. A. Spong, Phys. Plasmas **18**, 056109 (2011).
[15]W. W. Heidbrink and G. J. Sadler, Nucl. Fusion **34**, 535 (1994).
[16]M. Gobbin, G. Spizzo, L. Marrelli, and R. B. White, Phys. Rev. Lett. **105**, 195006 (2010).

[17]P. J. Bonofiglo, J. K. Anderson, M. Gobbin, D. A. Spong, J. Boguski, E. Parke, J. Kim, and J. Egedal, "Fast ion transport in the three-dimensional reversed-field pinch," Phys. Rev. Lett. (unpublished).
[18]J. J. Koliner, C. B. Forest, J. S. Sarff, J. K. Anderson, D. Liu, M. D. Nornberg, J. Waksman, L. Lin, D. L. Brower, W. X. Ding, and D. A. Spong, Phys. Rev. Lett. **109**, 115003 (2012).
[19]W. W. Heidbrink, Phys. Plasmas **15**, 055501 (2008).
[20]P. J. Bonofiglo (2018). "Fast ion transport in the quasi-single helical reversed-field pinch raw figure data," Zenodo, http://dx.doi.org/10.5281/zenodo.2547914
[21]L. Lin, W. X. Ding, D. L. Brower, J. J. Koliner, S. Eilerman, J. A. Reusch, J. K. Anderson, M. D. Nornberg, J. S. Sarff, J. Waksman, and D. Liu, Phys. Plasmas **20**, 030701 (2013).
[22]L. Lin, J. K. Anderson, D. L. Brower, W. Capecchi, W. X. Ding, S. Eilerman, C. B. Forest, J. J. Koliner, D. Liu, M. D. Nornberg, J. Reusch, and J. S. Sarff, Phys. Plasmas **21**, 056104 (2014).
[23]D. A. Spong, Phys. Plasmas **10**, 3217 (2003).
[24]J. D. Hanson, S. P. Hirshman, S. F. Knowlton, L. L. Lao, E. A. Lazarus, and J. M. Shields, Nucl. Fusion **49**, 075031 (2009).
[25]J. J. Koliner, M. R. Cianciosa, J. Boguski, J. K. Anderson, J. D. Hanson, B. E. Chapman, D. L. Brower, D. J. Den Hartog, W. X. Ding, J. R. Duff, J. A. Goetz, M. McGarry, L. A. Morton, and E. Parke, Phys. Plasmas **23**, 032508 (2016).
[26]W. Capecchi, J. K. Anderson, P. J. Bonofiglo, J. Kim, R. M. Magee, R. McConnell, E. Parke, and J. S. Sarff, "A measure of fast ion beta at marginal stability in the reversed field pinch," Rev. Nucl. Fusion (unpublished).
[27]S. Munaretto, B. E. Chapman, M. D. Nornberg, J. Boguski, A. M. DuBois, A. F. Almagri, and J. S. Sarff, Phys. Plasmas **23**, 056104 (2016).
[28]S. Munaretto, B. E. Chapman, D. J. Holly, M. D. Nornberg, R. J. Norval, D. J. Den Hartog, J. A. Goetz, and K. J. McCollam, Plasma Phys. Controlled Fusion **57**, 104004 (2015).
[29]W. W. Heidbrink, J. Kim, and R. J. Groebner, Nucl. Fusion **28**, 1897 (1988).
[30]R. B. White and M. S. Chance, Phys. Fluids **27**, 2455 (1984).
[31]A. B. Rechester and M. N. Rosenbluth, Phys. Rev. Lett. **40**, 38 (1978).
[32]M. Landreman and P. J. Catto, Phys. Plasmas **19**, 056103 (2012).
[33]J. A. Derr and J. L. Shohet, Phys. Rev. Lett. **43**, 1730 (1979).
[34]J. R. Cary and S. G. Shasharina, Phys. Plasmas **4**, 3323 (1997).
[35]H. E. Mynick, T. K. Chu, and A. H. Boozer, Phys. Rev. Lett. **48**, 322 (1982).
[36]J. M. Canik, D. T. Anderson, F. S. B. Anderson, K. M. Likin, J. N. Talmadge, and K. Zhai, Phys. Rev. Lett. **98**, 085002 (2007).
[37]J. M. Canik, D. T. Anderson, F. S. B. Anderson, C. Clark, K. M. Likin, J. N. Talmadge, and K. Zhai, Phys. Plasmas **14**, 056107 (2007).
[38]R. L. Bovin, S. J. Zweben, and R. B. White, Nucl. Fusion **33**, 449 (1993).
[39]M. R. Stoneking, J. T. Chapman, D. J. Den Hartog, S. C. Prager, and J. S. Sarff, Phys. Plasmas **5**, 1004 (1998).
[40]D. Terranova, T. Bolzonella, S. Cappello, P. Innocente, L. Marrelli, and R. Pasqualotto, Plasma Phys. Controlled Fusion **42**, 843 (2000).